Geophysical Journal International

Geophys. J. Int. (2015) **200,** 1012–1028
GJI Geodynamics and tectonics

doi: 10.1093/gji/ggu449

An iterative spectral solution method for thin elastic plate flexure with variable rigidity

Emmanuel S. Garcia,[1] David T. Sandwell[1] and Karen M. Luttrell[2]

[1]*Scripps Institution of Oceanography, University of California, San Diego, La Jolla, CA* 92093-0225, *USA. E-mail: esg006@ucsd.edu*
[2]*Department of Geology and Geophysics, Louisiana State University, Baton Rouge, LA* 70803, *USA*

Accepted 2014 November 14. Received 2014 September 18; in original form 2014 July 1

SUMMARY

Thin plate flexure theory provides an accurate model for the response of the lithosphere to vertical loads on horizontal length scales ranging from tens to hundreds of kilometres. Examples include flexure at seamounts, fracture zones, sedimentary basins and subduction zones. When applying this theory to real world situations, most studies assume a locally uniform plate thickness to enable simple Fourier transform solutions. However, in cases where the amplitude of the flexure is prominent, such as subduction zones, or there are rapid variations in seafloor age, such as fracture zones, these models are inadequate. Here we present a computationally efficient algorithm for solving the thin plate flexure equation for non-uniform plate thickness and arbitrary vertical load. The iterative scheme takes advantage of the 2-D fast Fourier transform to perform calculations in both the spatial and spectral domains, resulting in an accurate and computationally efficient solution. We illustrate the accuracy of the method through comparisons with known analytic solutions. Finally, we present results from three simple models demonstrating the differences in trench outer rise flexure when 2-D variations in plate rigidity and applied bending moment are taken into account. Although we focus our analysis on ocean trench flexure, the method is applicable to other 2-D flexure problems having spatial rigidity variations such as seamount loading of a thermally eroded lithosphere or flexure across the continental–oceanic crust boundary.

Key words: Numerical approximations and analysis; Lithospheric flexure; Mechanics, theory, and modelling.

1 INTRODUCTION

The oceanic lithosphere has an almost uniform composition and a well-understood thermal evolution away from spreading ridges (Parsons & Sclater 1977). Simple thermal evolution models, combined with isostasy and thin plate flexure theory, form the foundational methodology for understanding the gravity and topography of the deep oceans (Watts 2001). Examples include flexure at seamounts (Kim & Wessel 2010), spreading ridges (Luttrell & Sandwell 2012), fracture zones (Sandwell & Schubert 1982), continental margins (Erickson 1993) and most importantly subduction zones (Watts & Talwani 1974; Parsons & Molnar 1976; Levitt & Sandwell 1995; Bry & White 2007). In most of these cases, the flexural modelling uses a uniform-thickness plate (or, in some instances, a plate with smooth thickness variations over wavelengths greater than the flexural wavelength) because it is theoretically simple, computationally fast and usually provides an adequate description of the data if the results are interpreted in terms of an effective elastic thickness (Goetze & Evans 1979; McNutt & Menard 1982).

Over the past decade there have been dramatic improvements in the accuracy of the marine gravity field from satellite altimetry (Sandwell *et al.* 2013). In addition, the multibeam coverage of the seafloor topography has expanded. Inverse spectral techniques have been used to estimate elastic thickness of the oceanic lithosphere by examining the admittance and coherence between gravity and topography measurements (Kirby 2014). The spatial resolution of these estimates can be increased by using either wavelets (Kirby & Swain 2011), multitapers (Pérez-Gussinyé *et al.* 2009) or a convolution method (Braitenberg *et al.* 2002). However, variations in rigidity may occur over short spatial scales that are smaller than the typical flexural wavelength of a uniform rigidity plate. There is now an advanced understanding of the fracturing that occurs on the outer trench walls of subduction zones when the plates are bent beyond their elastic limits (e.g. Massell 2002; Ranero *et al.* 2003). Therefore, realistic models, which account for spatial variations in rigidity arising from the combination of along-trench age gradients and inelastic yielding on the outer trench wall are needed to explain the improved seafloor data.

Most previous studies on trench flexure have adopted an elastic rheology and focused on reproducing profiles along one dimension perpendicular to the trench (Hanks 1971; Watts & Talwani 1974; Caldwell *et al.* 1976; Bodine & Watts 1979; Levitt &

Sandwell 1995). However, in an attempt to explain the misfit in results for some trenches, other rheologies have been proposed for the oceanic lithosphere that account for perfectly plastic (Lobkovsky & Sorokhtin 1976), elastic-perfectly plastic (Turcotte *et al.* 1978), viscoelastic (Melosh 1978) or fully viscous behaviour (de Bremaecker 1977). One approach that allows plate rheology and failure condition to vary with depth is to construct a yield strength envelope (Goetze & Evans 1979; McNutt & Menard 1982). In this formulation, brittle failure in the upper, colder portion of the lithosphere together with ductile flow in the lower, hotter portion serve to constrain the thickness of an unyielded layer in the middle of the plate that behaves elastically. This effective elastic thickness T_e can be related to the flexural rigidity D of a thin plate, given a Young's modulus E and Poisson's ratio ν, through the relation

$$D(x, y) = \frac{E T_e^3(x, y)}{12(1 - \nu^2)}. \tag{1}$$

By letting the effective elastic thickness, or more generally the flexural rigidity, serve as a proxy for a more complete description of oceanic lithosphere rheology, we are able to adopt a thin elastic plate model for lithospheric flexure. In doing so, we can mathematically capture the gross behaviour of a plate with varying and non-elastic rheology without having to specify an exact rheological structure. At well-studied outer rise regions, high-resolution multibeam bathymetry data (Massell 2002), seismic refraction profiles (Ranero *et al.* 2003) and focal mechanism orientations (Craig *et al.* 2014) indicate pervasive extensional faulting. This increased yielding at the top of the plate decreases the plate's effective elastic thickness and hence flexural rigidity. As such, it is important to develop a computational model which includes variable rigidity in thin elastic plate flexure. In particular, 2-D variation is likely to be significant in some instances.

For example, elastic plates with variable rigidity in two dimensions were used to model the deformation of continental lithosphere in rifted basins (van Wees & Cloetingh 1994) and foreland basins (Garcia-Castellanos 2002). Flexure of the oceanic lithosphere at the trench outer rise has also been modelled using variable rigidity (Manriquez *et al.* 2014). These studies all noted the importance of including realistic variations in rigidity for successfully matching the observed topography (or bathymetry) with the output of their computational models. In the first two examples, the governing flexural equations were solved using finite difference techniques, while a finite element approach was taken in the last case. In this work, we present a method that solves the flexural equations by iteration in the spectral domain.

This iterative spectral method was originally developed in one dimension to model elastic flexure at oceanic fracture zones (Sandwell 1984), and has been further extended to 2-D applications for other geophysical problems dealing with inhomogeneous elastic media (Barbot *et al.* 2008; Luttrell & Sandwell 2012). Our method is able to obtain sufficiently accurate solutions for the deflection of a thin elastic plate with variable rigidity in two dimensions subject to arbitrary vertical loading and constant in-plane forces. When restrictions on the scale and amplitude of the variations in plate rigidity are followed, the iterative scheme converges rapidly. The high computational speed of our model is an advantage because it allows for finer grid spacing. Direct comparisons between model output and high-resolution data can be carried out without resorting to interpolation. Similarly, wider or more extensive searches for parameter values would then be possible for inverse problems.

In the following sections, we describe the mathematical framework of our computational scheme, and then report on its performance with respect to benchmark tests based on available analytic solutions. Finally, we demonstrate the potential utility of such a scheme by discussing some example cases of lithosphere flexure in a downgoing oceanic slab with varying rigidity or an arcuate trench shape and the subduction of a plate of varying age subject to inelastic yielding.

2 THEORY

Consider a thin elastic plate extending infinitely along two horizontal dimensions x and y. The plate's flexural rigidity $D(x, y)$ is in general a spatially varying function, and the plate is floating on an inviscid fluid substratum. The upward deflection of the plate surface $w(x, y)$ is the flexural response to the application of a vertical load distribution $p(x, y)$ and a constant in-plane force with components N_x, N_y and N_{xy}. The values of these in-plane forces are taken to be positive when the plate is subject to tension, and negative when it is under compression. Furthermore, a restoring force is exerted by the material of the substratum. This force is proportional to the acceleration due to gravity g and the density contrast $\Delta\rho$ between the substratum and the material in-fill above the plate.

The partial differential equation describing the vertical flexural deflection w of the plate can then be written as:

$$\begin{aligned}\nabla^2\left[D\nabla^2 w\right] - (1-\nu) \\ \times\left[\frac{\partial^2 D}{\partial x^2}\frac{\partial^2 w}{\partial y^2} - 2\frac{\partial^2 D}{\partial x\partial y}\frac{\partial^2 w}{\partial x\partial y} + \frac{\partial^2 D}{\partial y^2}\frac{\partial^2 w}{\partial x^2}\right] \\ -N_x\frac{\partial^2 w}{\partial x^2} - 2N_{xy}\frac{\partial^2 w}{\partial x\partial y} - N_y\frac{\partial^2 w}{\partial y^2} + \Delta\rho g w = p.\end{aligned} \tag{2}$$

The boundary conditions are such that the deflection w vanishes at infinity,

$$\lim_{|x|,|y|\to\infty} w = 0 \tag{3}$$

as should the slopes of the deflection along the corresponding dimensions:

$$\lim_{|x|\to\infty}\frac{\partial w}{\partial x} = 0, \quad \lim_{|y|\to\infty}\frac{\partial w}{\partial y} = 0. \tag{4}$$

When the rigidity D has a spatially uniform value D_0, the solution for 2-D flexure of a plate with uniform rigidity D_0 subjected to arbitrary vertical and in-plane loads may be written in the wavenumber domain of k_x and k_y (Banks *et al.* 1977; Wessel 1996). Denoting the Fourier transform of the deflection $\mathcal{F}[w(x, y)]$ by $\hat{w}(k_x, k_y)$, the uniform plate solution can be written as

$$\hat{w}_0(k_x, k_y) = \hat{p}(k_x, k_y)\hat{\Phi}(k_x, k_y), \tag{5}$$

where we have defined a 'uniform response function' $\hat{\Phi}(k_x, k_y)$:

$$\begin{aligned}\hat{\Phi}(k_x, k_y) = \Big[(2\pi)^4 D_0\left(k_x^2 + k_y^2\right)^2 + (2\pi)^2 \\ \times\left(N_x k_x^2 + 2N_{xy}k_x k_y + N_y k_y^2\right) + \Delta\rho g\Big]^{-1}.\end{aligned} \tag{6}$$

The thin elastic plate formulation as expressed in (2) is valid when the rigidity $D(x, y)$ is slowly varying. To make this requirement explicit, the form of the rigidity must be such that it can be decomposed into a spatially uniform value D_0 and a spatially variable part $D'(x, y)$,

$$D(x, y) = D_0 + D'(x, y). \tag{7}$$

By using the decomposition in (7), we can rewrite (2) as an integral equation in the wavenumber domain,

$$\hat{w}(k_x, k_y) = \hat{p}(k_x, k_y)\hat{\Phi}(k_x, k_y) - (2\pi)^4 \left\{ \int_{-\infty}^{+\infty} \int_{-\infty}^{+\infty} \mathrm{d}s_x \, \mathrm{d}s_y \, \hat{D}'(k_x - s_x, k_y - s_y)\hat{w}(s_x, s_y) \times \left\{ \left(k_x^2 + k_y^2\right)\left(s_x^2 + s_y^2\right) - (1-\nu) \times \left[(k_x - s_x)^2 s_y^2 - 2(k_x - s_x)(k_y - s_y)s_x s_y + (k_y - s_y)^2 s_x^2\right] \right\} \right\}. \quad (8)$$

We show in Appendix A that (8) is in the form of a 2-D Fredholm integral equation of the second kind, and may be solved through an iterative process as described in Appendix B. Our iterative solution to this problem for arbitrary, square-integrable rigidity D and load distribution p is developed using Fourier transforms in the wavenumber domain, but some calculations are performed in the space domain to improve accuracy and execution time. The iteration that is implemented in our computer algorithm is

$$\hat{w}^{(n)}(k_x, k_y) = \hat{w}_0(k_x, k_y) - \hat{\Phi}(k_x, k_y)\mathcal{F}\left\{ \nabla^2 \left[D'\nabla^2 w^{(n-1)}\right] - (1-\nu)\left[\frac{\partial^2 D'}{\partial x^2}\frac{\partial^2 w}{\partial y^2}^{(n-1)} - 2\frac{\partial^2 D'}{\partial x \partial y}\frac{\partial^2 w}{\partial x \partial y}^{(n-1)} + \frac{\partial^2 D'}{\partial y^2}\frac{\partial^2 w}{\partial x^2}^{(n-1)} \right] \right\}. \quad (9)$$

An updated solution $\hat{w}^{(n)}$ in the wavenumber domain is equal to the uniform plate solution $\hat{w}_0$ that is corrected by a small perturbation related to the spatial derivatives of the varying part of the rigidity D', as well as the spatial derivatives of the previous solution $w^{(n-1)}$. The iteration is allowed to continue until the root mean square differences between successive solution estimates w_n and w_{n-1} drop below a specified tolerance value. The boundary conditions (3) and (4) are enforced by setting the mean value of plate deflection to zero which corresponds to setting the zero wavenumber component to zero. In addition, the applied load distribution p must have zero mean.

While the differential equation and boundary conditions could be solved in the space domain using a finite difference or finite element approach, the Fourier analysis is helpful in four areas. (1) The Fourier approach provides an optimal initial guess as the well-known solution to flexure of a uniform rigidity plate under an arbitrary load (Banks *et al.* 1977; Wessel 1996). (2) For periodic band-limited functions $D'(x, y)$ and $w(x, y)$, the most accurate estimates of the derivatives with respect to x and y are performed by wavenumber multiplication in the Fourier domain (Trefethen 2000). One could design an optimal finite difference operation in the space domain to perform the derivative, but as shown in (Trefethen 2000), the length of that space domain operator is equal to the length of the w or D' arrays. The most accurate and efficient way to perform this differentiation is by taking the discrete Fourier transform of each array, multiplying by the appropriate wavenumbers, and then inverse transforming the result. The three terms involving spatial derivatives of the D' array need to be evaluated only once while the three spatial derivatives of the w array need to be evaluated at each iteration. (3) By iterating in the Fourier domain, the band-limited requirement for convergence can be enforced by suppressing numerical instabilities that can occur at the shortest wavelengths. (4) Finally, the conditions for convergence of the iterative scheme are best exposed in the Fourier domain as shown in Appendix C.

3 BENCHMARKS

We tested the accuracy of the iterative algorithm given in eq. (9) through comparisons with analytic, closed-form solutions to thin plate flexure problems. As there is a paucity of such solutions in two dimensions which involve variable rigidity, we drew most benchmark cases from textbook examples of 1-D solutions (Hetenyi 1946; Turcotte & Schubert 2002). The numerical algorithm was coded in FORTRAN and utilizes a multidimensional fast Fourier transform (FFT) routine written by Brenner (1967). The inputs to the program are grids of plate rigidity $D(x, y)$ and the load distribution $p(x, y)$. The program calculates grids of plate deflection, plate curvature and gravity anomaly as output. Typical grid sizes are 2048 × 2048 pixels and grid spacing is about one hundredth of the flexural wavelength so most cases had grid sizes of 20 flexural wavelengths across both grid dimensions. Such spatially large grids are needed to ensure that the numerical solutions approach zero at the boundaries.

The benchmark results, (a) through (g), are summarized in Fig. 1. The first column of the figure provides a short description of the benchmark as well as the equation in this section for the analytic formula. The second column shows the loading configurations of benchmarks in diagrams. Note all these cases are 1-D benchmarks except for (f). Also note that only benchmarks (b) and (g) have variable rigidity. The third column shows profiles of plate deflection taken across each model where the horizontal scale is normalized by the appropriate flexural parameter. At this vertical scale the profiles from the numerical models and analytic solutions cannot be distinguished. The last column shows the difference between the numerical and analytic solutions, which range from about 1 to 10 per cent depending on the benchmark.

(a) Line load, uniform D

The first benchmark is a line load on a plate with uniform rigidity D_0 (Fig. 1a). The load distribution has the form $p(x, y) = V_0\delta(x)$, where V_0 is the amplitude of the vertical load. The upward deflection $w(x)$ then has the expression (Hetenyi 1946; Turcotte & Schubert 2002):

$$w = -w_l \exp\left(-\frac{|x|}{\alpha}\right)\left[\cos\left(\frac{x}{\alpha}\right) + \sin\left(\frac{|x|}{\alpha}\right)\right], \quad (10)$$

where the amplitude is $w_l = V_0\alpha^3/8D_0$ and the flexural parameter α is given by

$$\alpha = \left[\frac{4D_0}{\Delta\rho g}\right]^{1/4}. \quad (11)$$

In this case as well as the other tests that followed, we assumed a density contrast $\Delta\rho$ that is appropriate for the oceanic lithosphere, where the substrate has a density similar to that of the uppermost mantle and the in-fill above the plate has the density of seawater.

We use our numerical approach to simulate this simple case. The difference between the analytic and numerical solutions are everywhere smaller than 1 per cent. The difference is caused by the finite length of the numerical model and could be improved by increasing the x-dimension of the model.

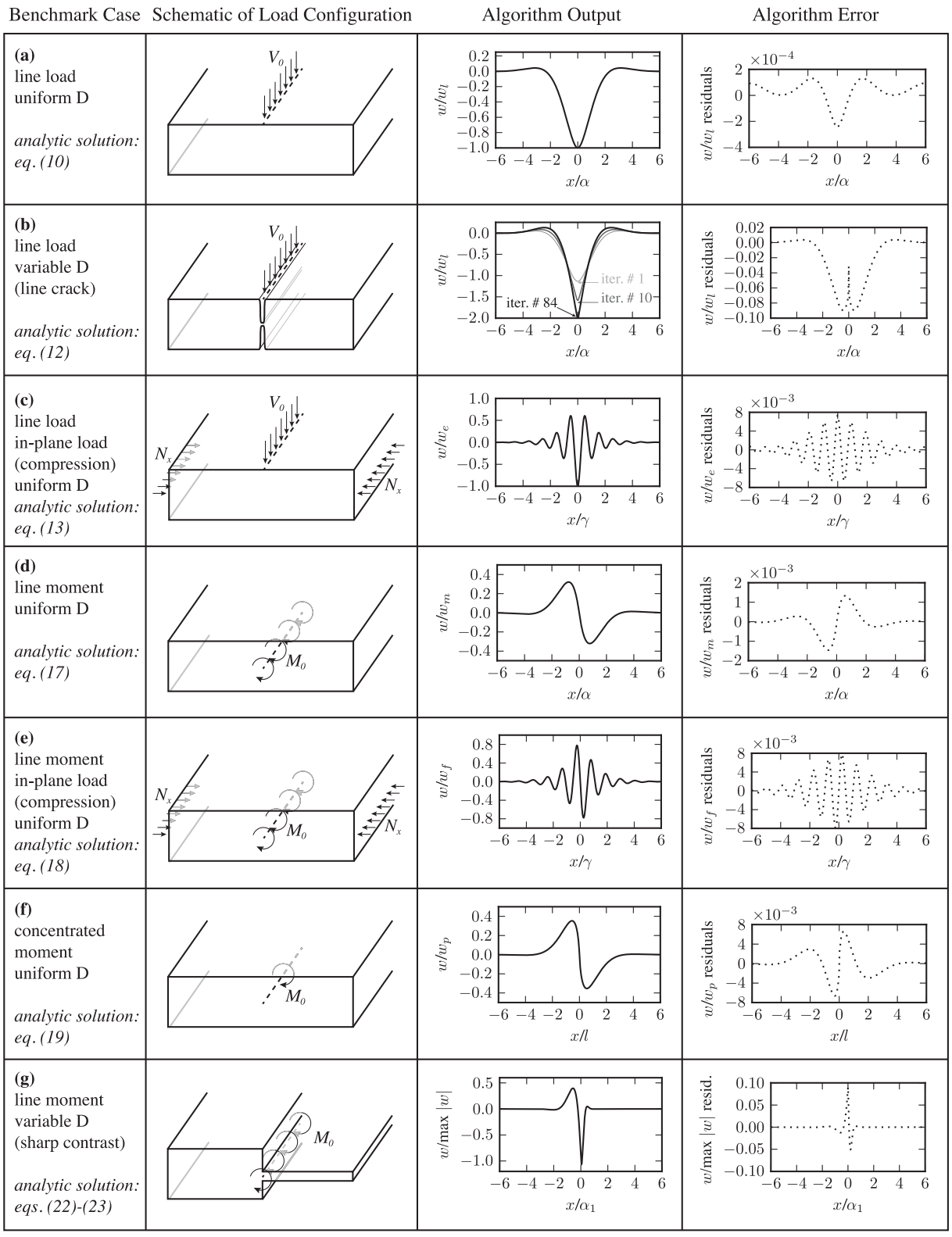

Figure 1. Summary of benchmark tests.

(b) Line load, variable D (line crack)

The second benchmark is a line load on a cracked plate (Fig. 1b). The analytic solution is (Watts 2001; Turcotte & Schubert 2002)

$$w = -2w_l \exp\left(-\frac{|x|}{\alpha}\right)\cos\left(\frac{x}{\alpha}\right), \tag{12}$$

where w_l and α have the same values as in (10). We model this broken plate as a sharp reduction in rigidity at the origin. In practice, the code will not converge if the rigidity contrast between the plate and the hole is greater than about 1000, corresponding to a reduction in elastic thickness by an order of magnitude. In addition the shape of the rigidity reduction was modelled using a Gaussian function

with a half width of 20 pixels while the load was 1 pixel wide. This finite width of the rigidity hole corresponds to smoothing the rigidity to enable convergence as discussed in Appendix C while still permitting variation over wavelengths considerably shorter than the flexural wavelength. The path to convergence is shown in Fig. 1(b). The first iteration provides a good fit to the uniform rigidity plate flexure solution. After 10 iterations the fit at the origin improves and by 84 iterations the solution has converged. The model error plot shows some large differences of up to 10 per cent between the converged numerical solution and the analytic solution (12). These are primarily due to the need to have a finite width flexural rigidity hole, which moves the region of maximum flexure by about 5 pixels away from the origin. This misfit illustrates the band-limited nature of this numerical modelling approach and demonstrates the error introduced when this smoothness constraint is not met.

(c) Line load, in-plane compression, uniform D

The third benchmark is a line load on a uniform rigidity plate (Fig. 1c). An additional constant compressional in-plane force N_x is applied along the x-direction. The analytic solution is (Hetenyi 1946):

$$w = -w_e \exp\left(-\frac{|x|}{\beta}\right)\left[\beta\cos\left(\frac{x}{\gamma}\right) + \gamma\sin\left(\frac{|x|}{\gamma}\right)\right], \tag{13}$$

where $w_e = V_0/2\alpha^2\Delta\rho g$ with α as in (11) and the other flexural parameters β and γ have the expressions

$$\beta = \left[\left(\frac{\Delta\rho g}{4D_0}\right)^{1/2} + \left(\frac{N_x}{4D_0}\right)\right]^{-1/2} \tag{14}$$

$$\gamma = \left[\left(\frac{\Delta\rho g}{4D_0}\right)^{1/2} - \left(\frac{N_x}{4D_0}\right)\right]^{-1/2}. \tag{15}$$

From the form of β and γ, we can identify the critical buckling load N_c as

$$N_c = 2\left(\Delta\rho g D_0\right)^{1/2}. \tag{16}$$

We tested both extensional and compressional regimes for our benchmarks, but here we show only one case in which the magnitude of the compressional in-plane force is $0.95N_c$ (Fig. 1c). The numerical model differs from the analytic formula by less than 1 per cent even when the loading conditions are close to inducing plate buckling.

(d) Line moment, uniform D

The fourth benchmark is a line moment on a uniform rigidity plate (Fig. 1d). The deflection w may be found by approximating the applied moment as a couple of equal and opposing vertical loads (Hetenyi 1946; Watts 2001). We illustrate the assumptions and implications of this approximation in Appendix D. Adapting the 1-D solution arising from this approximation for the case of a line moment applied along the y-direction on a plate leads to the expression

$$w = -w_m \exp\left(-\frac{|x|}{\alpha}\right)\sin\left(\frac{x}{\alpha}\right), \tag{17}$$

where $w_m = M_0\alpha^2/4D_0$. The numerical model differs from the analytic formula by less than 1 per cent for this case.

(e) Line moment, in-plane compression, uniform D

The fifth benchmark is a line moment on a uniform rigidity plate including an in-plane force (Fig. 1e). The deflection may be obtained as (Hetenyi 1946),

$$w = -w_f \exp\left(-\frac{|x|}{\beta}\right)\sin\left(\frac{x}{\gamma}\right), \tag{18}$$

where in this case $w_f = M_0\beta\gamma/4D_0$ and the same expressions for β and γ as in (14) and (15) are used. As with the previous example, the numerical model differs from the analytic formula by less than 1 per cent.

(f) Concentrated moment, uniform D

The sixth benchmark is a concentrated moment applied to a uniform rigidity plate (Fig. 1f). The moment is oriented along the x-direction and is applied at the origin. The deflection due to this concentrated moment is given by:

$$w = w_p\left[\frac{x}{2^{1/2}l\left(x^2+y^2\right)^{1/2}}\right]\left\{\mathrm{Kei}_1\left[\frac{\left(x^2+y^2\right)^{1/2}}{l}\right] - \mathrm{Ker}_1\left[\frac{\left(x^2+y^2\right)^{1/2}}{l}\right]\right\}, \tag{19}$$

where we are using Kelvin–Bessel functions Ker and Kei of order 1, and $w_p = V_0 l^2/2\pi D_0$. The flexural parameter l has the form,

$$l = \left[\frac{D_0}{\Delta\rho g}\right]^{1/4}. \tag{20}$$

The numerical model differs from the analytic formula by less than 1 per cent for this case as well.

(g) Line moment, variable D (sharp contrast)

The final benchmark is a line moment applied to a plate with a stepwise change in rigidity (Fig. 1g). The rigidity has a variation described by

$$D(x) = \begin{cases} D_1: & x < 0 \\ D_2: & x > 0 \end{cases} \tag{21}$$

and a line moment is applied along the boundary at $x = 0$ between the two regions of the plate. As derived in Appendix E, the formulas for the deflection w_1 and w_2 in each region are

$$w_1 = \exp\left(\frac{x}{\alpha_1}\right)\left[A_1\cos\left(\frac{x}{\alpha_1}\right) + B_1\sin\left(\frac{x}{\alpha_1}\right)\right]: \quad x < 0 \tag{22}$$

$$w_2 = \exp\left(-\frac{x}{\alpha_2}\right)\left[A_2\cos\left(\frac{x}{\alpha_2}\right) + B_2\sin\left(\frac{x}{\alpha_2}\right)\right]: \quad x > 0, \tag{23}$$

where α_1 and α_2 are the flexural parameters for the plate regions on each side of the boundary. The values for the coefficients A_1, A_2, B_1 and B_2 are given in Appendix E. The deflection computed by the iterative spectral method agrees to within 10 per cent with the analytic solutions for a rigidity contrast of a factor of 1000 (corresponding to a T_e contrast of ~10 times).

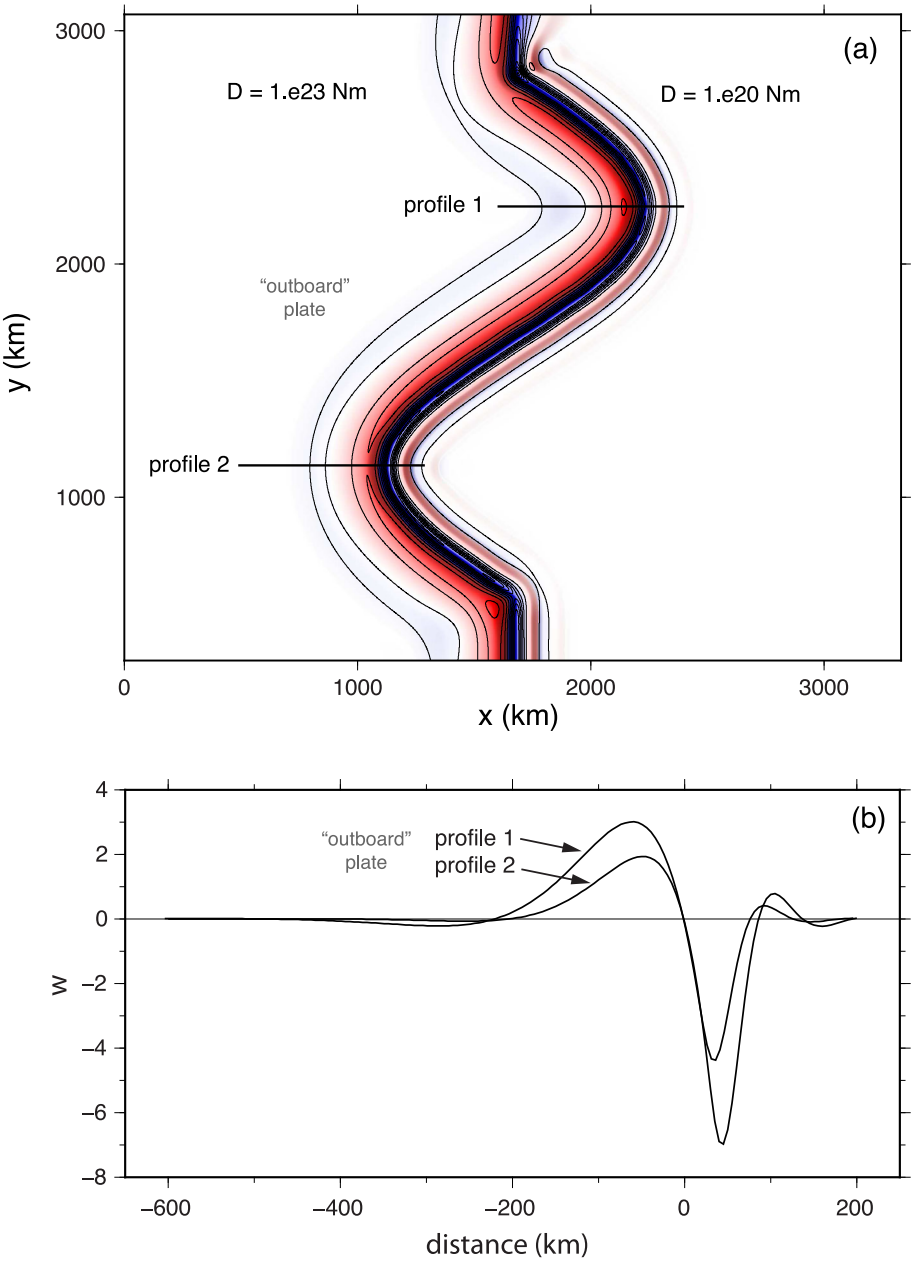

Figure 2. (a) Plate deflection due to a uniform bending moment applied to a trench having a sinusoidal planform. The flexural rigidity of the plate to the right-hand side of the trench is 1000 times less than the flexural rigidity on the left-hand side of the trench resulting in an asymmetry across the trench. Red colour indicates deflection upwards while blue colour indicates deflection downwards. Contours of deformation shown every 1 m. (b) Profiles across the most concave and convex parts of the trench illustrate the effects of curvature on the amplitude and wavelength of the flexure.

4 DISCUSSION

4.1 Example 2-D models

In the previous section, we evaluated the accuracy of the iterative spectral method through comparisons with analytic solutions, under a variety of the loading and rigidity configurations. We also examined the validity of the vertical load couple approximation to the effect of an applied moment in the plate interior. This new modelling approach is particularly appropriate for simulating plate flexure outboard of deep ocean trenches. The most general case of trench flexure has a plate of variable age, and thus variable flexural rigidity, being subducted along a trench that has an arcuate planform. The first two models presented in this study illustrate the importance of these two effects as well as the robustness of our solution algorithm by deliberately exaggerating the rigidity contrast and trench axis geometry. The computer algorithm can accommodate both effects simultaneously but we separate them to isolate their relative importance, then show their combined effects in the third and last model.

The first case illustrates the importance of an arcuate trench planform on trench depth and outer rise height. The model trench has a sinusoidal planform as shown in Fig. 2, representing an extreme case of an arcuate trench. A uniform bending moment of 1.0×10^{15} N was applied along the trench by constructing a 2-D force grid containing mostly zeros but having force couples that are

approximated by the derivative of a Gaussian function, effectively producing a force couple with a finite width of one pixel. The plate on the left-hand side of the trench was assigned a uniform flexural rigidity of 1.0×10^{23} Nm while the plate on the right-hand side was assigned a rigidity 1000 times smaller, corresponding to a T_e of 25 and 2.5 km, respectively. In an actual subduction zone, the subducted plate ends somewhere deep in the mantle. Our solution method is designed only for continuous plates where the deformation goes to zero at the edges of the model. To simulate the plate having an end in the mantle we dramatically weaken the subducted plate so its finite strength does not have a dominant effect on the flexure outboard of the trench. The sinusoidal model with variable rigidity was embedded in a larger 2048×2048 grid with a pixel spacing of 1.85 km. The larger grid has a uniform rigidity around the perimeter of the smaller subgrid. Convergence to an accuracy of better than 0.004 was achieved after 60 iterations in 130 s of CPU time on a personal computer.

The results (Fig. 2) illustrate the importance of accommodating a realistic trench planform as well as the ability to dramatically lower the flexural rigidity of the 'subducted' plate. Fig. 2 shows a contour plot of the plate deflection. Similarly as in (Tanimoto 1998), the physical interpretation of the 'outboard' deflection should be restricted to regions where the deflection curve is concave downward, which for Fig. 2(b) is to the right of 25 km for profile 1 and 50 km for profile 2. There, the flexure has a broader response than the flexure on the right-hand side of the trench. This is due to the 1000 times difference in flexural rigidity. By simulating a broken end of the subducted plate in the mantle in this way, the numerical values of the applied loads lose absolute physical meaning, but the deflection and curvature of the trench and outer rise are accurately preserved. Two profiles taken across the most concave (profile 1) and convex (profile 2) planforms of the trench illustrate the impact of trench curvature on both the amplitude and wavelength of the flexure. Profile 1 has an outer rise that is 1.5 times taller than profile 2 and the distances to the first zero crossing outboard of the outer rises are significantly different. If one modelled these two flexure profiles using the standard 1-D approach the estimates of bending moment and flexural rigidity for profile 1 would be too large while the same estimates for profile 2 would be too small. When modelling real seafloor topography data, the position of the trench and outer rise will depend on the location of the applied bending moment. The benchmarks provided above show that the location of the first zero crossing point seaward of the trench axis can be adjusted by changing the ratio of the downward load V_0 and the bending moment M_0 (Turcotte & Schubert 2002).

The second case illustrates the ability and importance of varying the flexural rigidity along the strike of the trench. When modelling actual trenches, the rigidity outboard of the trench will vary according to the rigidity expected for the actual age of the plate. In this model, the flexural rigidity varies smoothly over a range appropriate for oceanic lithosphere (T_e of 5–25 km) as shown in Fig. 3. This corresponds to an along-strike variation in rigidity of 125 times. Elastic thicknesses and flexural rigidity are provided along six sample profiles in Fig. 3. As in the previous case a uniform bending moment of 1.0×10^{15} N was applied along the trench by constructing a 2-D force grid and utilizing the derivative of a Gaussian to assign forces to pixels. The results show a reduction in flexural amplitude and an increase in flexural wavelength as the flexural rigidity is increased from the bottom to the top of the plate, as is expected in a plate with gradually varying rigidity.

The third and final case we present is a toy model of the expected plate deflection along a portion of the South America trench offshore Chile (Fig. 4a), using the actual trench geometry but synthetic estimates of the rigidity and loading properties. We caution the reader that it is outside of the scope of the present study to obtain rigorous estimates for these parameters that agree well with observations. For this toy model, the vertical loads and moments were applied along a digitized planform of the trench that was divided into 25-km-long segments. The magnitudes for this load distribution were chosen arbitrarily in order to reasonably simulate variations in loading along the Chile trench (Bry & White 2007; Contreras-Reyes & Osses 2010). The rigidity variations (shown in Figs 4e and f) outboard of the trench reflect a reasonable estimate of variations due to lithosphere age and plate weakening due to yielding, while the rigidity inboard of the trench was set to a constant value which is an order of magnitude lower. Note that the rigidity values assumed here will differ from those corresponding to previous estimates of effective elastic thickness for the outer rise at this particular region (Bry & White 2007; Contreras-Reyes & Osses 2010), in part due to the choice of thermal parameters. However, what we seek to demonstrate here is the significance of relative variations in rigidity. When lithospheric yielding is taken into account in our model, the plate can be as much as ten times weaker at the trench than otherwise. This in turn results in significant curvature of the model deflection at the outer rise that is not captured when plate rigidity varies only with age without any imposed weakening (Figs 4b and d). While the depth at the trench is about the same for both test cases, the outer rise is more prominent for the case that allows yielding. This model, though using synthetic rigidity and loading parameters, demonstrates the potential utility of our iterative solution to future studies involving flexural modelling, particularly those concerned with the curvature of the outer rise in subducting oceanic plates.

4.2 Some practical considerations

In all of the test cases and benchmark models described above, the load and rigidity are embedded in a grid having dimensions of a power of 2. In actuality, any grid having dimensions that can be factored into small prime numbers is nearly optimal for the FFT algorithm (Brenner 1967). One minor issue occurs at the boundaries of the model when there are sharp variations in rigidity. The Fourier analysis assumes all the functions repeat cyclically over the length and height of the grid. The rate of convergence of the iteration method depends on both the magnitude and rate of variation of the flexural rigidity grid. To improve convergence rate, the part of the rigidity grid that is external to the model area is smoothly tapered to a constant background value. Hence the rigidity along the perimeter of the total grid becomes set to a constant value as well. In addition the rigidity grid is low-pass filtered in the wavenumber domain using a Gaussian function to reduce the amplitudes of the transformed rigidity grid near the Nyquist wavenumber. The half-wavelength of this Gaussian filter is 10 pixels which is similar to the smoothing needed for the cracked plate benchmark.

While this paper is largely focussed on potential applications to modelling flexure outboard of trenches, the model formulation is quite general and could be applied to any thin-plate flexure problem where variable rigidity is needed. One case where this method (1-D) was already used is to model the flexural evolution of an oceanic fracture zone where a step contrast in age across the fracture zone results in a sharp contrast in flexural rigidity (Sandwell 1984). The young side of the fracture zone subsides at a faster rate than the older side and this differential subsidence drives the flexure. Another potential example is the modelling of flexure beneath

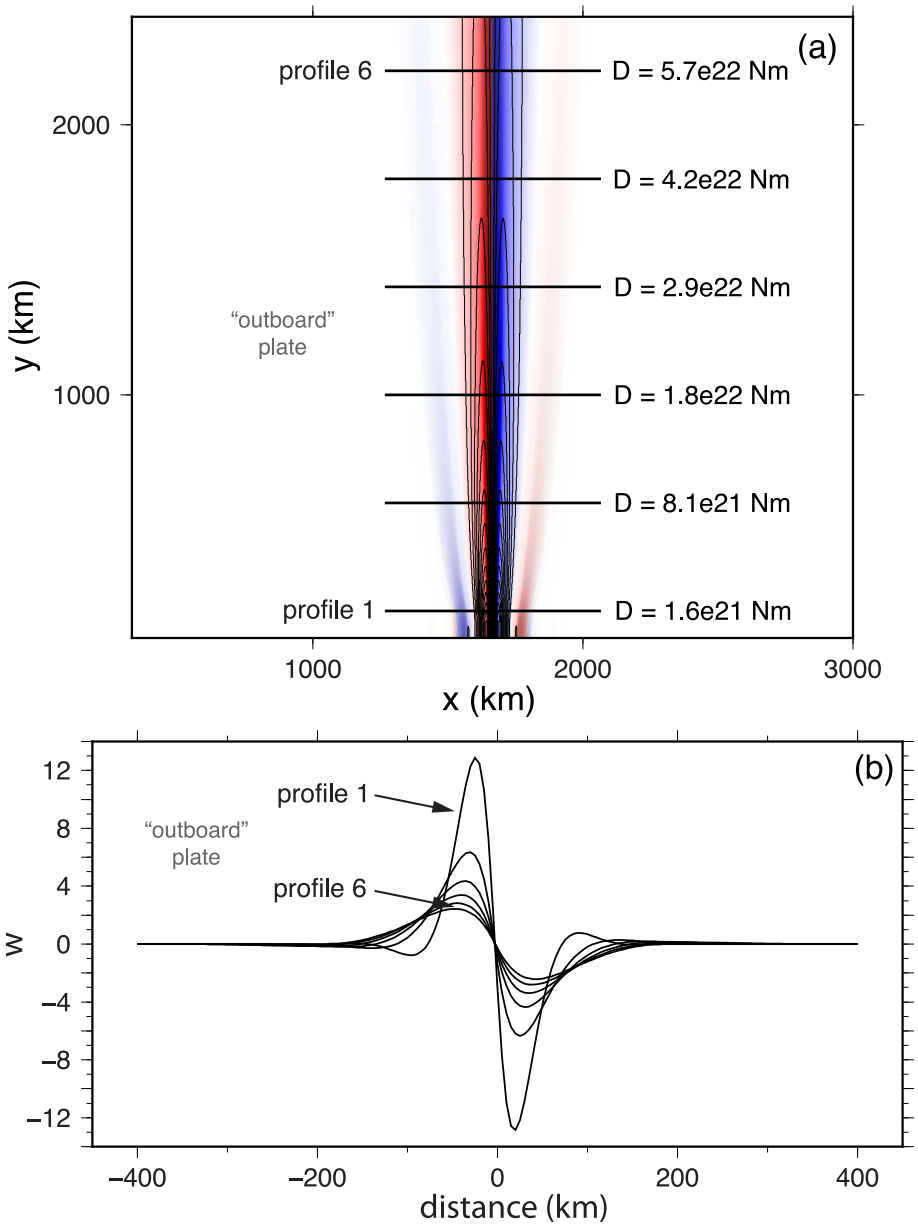

Figure 3. Plate deflection due to a uniform line moment applied to a plate of spatially variable rigidity. (a) The rigidity variations from the bottom to the top of the plate correspond to elastic thickness variations appropriate for oceanic lithosphere (5–25 km). Red colour indicates deflection upwards while blue colour indicates deflection downwards. Contours of deformation shown every 1 m. (b) Six profiles extracted from the plate deflection model illustrate the changes in amplitude and flexural wavelength due to along-strike variations in rigidity.

very large seamounts which have bent the plate beyond its elastic limits. Accordingly, a cracked plate model has been proposed for the Hawaiian Chain (Watts 2001). A third potential application is the flexure of foreland basins where the amplitude of the flexure is sufficient to weaken the plate (Watts 2001). Indeed this formulation could be used to model any type of thin plate flexure where the size of the plate is much greater than the flexural wavelength such that the boundary conditions given in eqs (3) and (4) are appropriate.

5 CONCLUSIONS

We have developed a 2-D iterative spectral method to compute the flexural response of a thin elastic plate of variable rigidity floating on an inviscid fluid half-space that is subjected to an arbitrary vertical load and in-plane force. The method will converge as long as the spatial variations in flexural rigidity are band-limited. In practice, we note that the rigidity grid must be low-pass filtered over a distance of about 10 pixels to achieve convergence.

We have assembled seven analytical benchmarks for testing the code. Five of these benchmarks have uniform rigidity plates so accurate solutions are achieved in one iteration. The two non-uniform rigidity benchmarks correspond to a broken plate and a plate with a step in rigidity. The numerical result for the 1000-times step variation in rigidity shows excellent agreement with the analytic solution while there are up to 10 per cent differences between the numerical broken plate result and its analytic solution. This broken plate case reveals the limitation of the approach in that the rigidity must

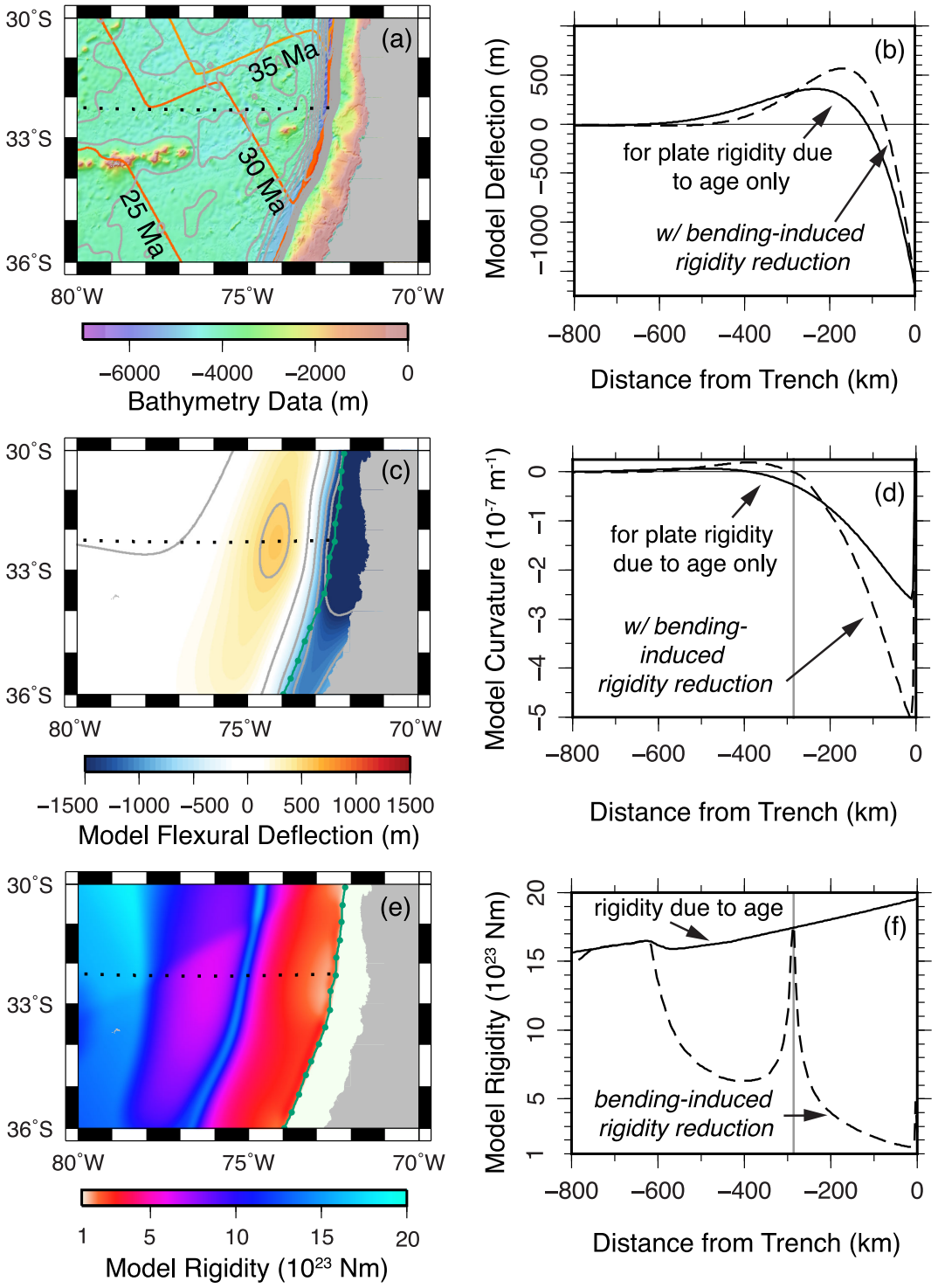

Figure 4. Plate deflection due to a varying moment and vertical load applied to a plate of spatially variable rigidity based on plate age and lithospheric yield strength envelopes. (a) Map of high-resolution multibeam and predicted bathymetry (Smith & Sandwell 1997) with contours every 500 m from depths of 4 to 6 km. Contours of seafloor age (Müller *et al.* 2008) every 5 Ma are also shown. (b) Profiles of flexural deflection are compared for the cases when the plate rigidity is only based on age, and when weakening from increased curvature due to bending occurs. The location of the profile is shown as a dotted track in the maps along the left-hand panel. (c) Model results for flexural deflection, with contours every 500 m. The moment and vertical loads were applied along the trench planform outlined in dark green. (d) Profiles of the deflection curvature (second spatial derivative). (e) The rigidity grid used to compute the final deflection solution displays some weakening towards the trench, with cooler colours representing a stronger plate and warmer colours corresponding to a weaker plate. The transition from cool to warm colours occurs around the mean value of the rigidity for this grid, which is around 5×10^{23} Nm. (f) Rigidity values along the profile are compared. The sharp spike upwards in rigidity around 300 km away from the trench corresponds to a change in the sign of the curvature.

be smooth relative the Nyquist wavelength, but can still vary over wavelengths shorter than the flexural wavelength. For Earth applications we expect smooth spatial variations in rigidity in this range so the accuracy of the solutions should be better than 10 per cent.

To illustrate the 2-D capabilities of the approach we considered three variable rigidity test cases to simulate subduction zones. The first case has a sinusoidal trench planform and dramatic weakening of the 'subducted' plate. The results show a factor of 1.5 difference in outer rise height on the plate outboard of the concave trench planform relative to the plate outboard of the convex trench planform. This highlights the need to have a 2-D formulation for modelling actual trenches. The second case is a linear trench where the subducting plate has an along-trench ramp in elastic thickness from 5 to 25 km. As expected the flexural profiles across the trench vary dramatically with the underlying plate thickness. In the third case, we have combined these two features to simulate a more realistic subduction geometry with a synthetic model of the Chile trench, offshore South America. This final model demonstrates the utility we expect this solution to bring to flexural modelling studies in the future.

Finally, we note that the vertical loading grid and rigidity grids can be arbitrarily complex as long as they satisfy the smoothness needed for convergence. Therefore this approach could be applied to all types of geophysical flexure problems ranging from seamount loading to thermomechanical evolution of sedimentary basins.

ACKNOWLEDGEMENTS

We thank the editor Jörg Renner and two anonymous reviewers for their instructive evaluation of the manuscript. Rachel Marcuson and Matt Siegfried provided constructive comments on early drafts. Pål Wessel served as an invaluable resource on flexural modelling. This research was supported by the National Science Foundation (OCE-1128801), the Office of Naval Research (N00014-12-1-0111), and ConocoPhillips.

REFERENCES

Banks, R.J., Parker, R.L. & Huestis, S.P., 1977. Isostatic compensation on a continental scale: local versus regional mechanisms, *Geophys. J. Int.,* **51**(2), 431–452.

Barbot, S., Fialko, Y. & Sandwell, D., 2008. Effect of a compliant fault zone on the inferred earthquake slip distribution, *J. geophys. Res.,* **113**(B6), doi:10.1029/2007JB005256.

Bodine, J. & Watts, A., 1979. On lithospheric flexure seaward of the Bonin and Mariana trenches, *Earth planet. Sci. Lett.,* **43**(1), 132–148.

Braitenberg, C., Ebbing, J. & Götze, H.-J., 2002. Inverse modelling of elastic thickness by convolution method the Eastern Alps as a case example, *Earth planet. Sci. Lett.,* **202**(2), 387–404.

Brenner, N., 1967. Three FORTRAN programs that perform the Cooley-Tukey Fourier transform, Tech. rep., DTIC Document.

Brotchie, J.F., 1971. Flexure of a liquid-filled spherical shell in a radial gravity field, *Modern Geol.,* **3,** 15–23.

Bry, M. & White, N., 2007. Reappraising elastic thickness variation at oceanic trenches, *J. geophys. Res.,* **112**(B8), doi:10.1029/2005JB004190.

Caldwell, J.G., Haxby, W.F., Karig, D.E. & Turcotte, D.L., 1976. On the applicability of a universal elastic trench profile, *Earth planet. Sci. Lett.,* **31**(2), 239–246.

Contreras-Reyes, E. & Osses, A., 2010. Lithospheric flexure modelling seaward of the Chile trench: implications for oceanic plate weakening in the trench outer rise region, *Geophys. J. Int.,* **182**(1), 97–112.

Craig, T.J., Copley, A. & Jackson, J., 2014. A reassessment of outer-rise seismicity and its implications for the mechanics of oceanic lithosphere, *Geophys. J. Int.,* **197**(1), 63–89.

de Bremaecker, J.-C., 1977. Is the oceanic lithosphere elastic or viscous?, *J. geophys. Res.,* **82**(14), 2001–2004.

Erickson, S.G., 1993. Sedimentary loading, lithospheric flexure, and subduction initiation at passive margins, *Geology,* **21**(2), 125–128.

Garcia-Castellanos, D., 2002. Interplay between lithospheric flexure and river transport in foreland basins, *Basin Res.,* **14**(2), 89–104.

Goetze, C. & Evans, B., 1979. Stress and temperature in the bending lithosphere as constrained by experimental rock mechanics, *Geophys. J. Int.,* **59**(3), 463–478.

Hanks, T.C., 1971. The Kuril trench—Hokkaido Rise system: large shallow earthquakes and simple models of deformation, *Geophys. J. Int.,* **23**(2), 173–189.

Hetenyi, M., 1946. *Beams on Elastic Foundation: Theory with Applications in the Fields of Civil and Mechanical Engineering,* The University of Michigan Press.

Jerri, A.J., 1999. *Introduction to Integral Equations with Applications,* 2nd edn, Wiley.

Kim, S.-S. & Wessel, P., 2010. Flexure modelling at seamounts with dense cores: flexure modelling with dense core loads, *Geophys. J. Int.,* **182**(2), 583–598.

Kirby, J. & Swain, C., 2011. Improving the spatial resolution of effective elastic thickness estimation with the fan wavelet transform, *Comput. Geosci.,* **37**(9), 1345–1354.

Kirby, J.F., 2014. Estimation of the effective elastic thickness of the lithosphere using inverse spectral methods: the state of the art, *Tectonophysics,* **631,** 87–116.

Korevaar, J., 1968. *Mathematical Methods,* Academic Press.

Lambeck, K. & Nakiboglu, S.M., 1980. Seamount loading and stress in the ocean lithosphere, *J. geophys. Res.,* **85**(B11), 6403–6418.

Levitt, D.A. & Sandwell, D.T., 1995. Lithospheric bending at subduction zones based on depth soundings and satellite gravity, *J. geophys. Res.,* **100**(B1), 379–400.

Lobkovsky, L.I. & Sorokhtin, O.G., 1976. Plastic deformation of oceanic lithosphere in a subduction zone, in *Tectonics of Lithospheric Plates,* pp. 22–52, ed. Sorokhtin, O.G., Institut Okeanologii Akad. Nauk SSSR.

Luttrell, K. & Sandwell, D., 2012. Constraints on 3-D stress in the crust from support of mid-ocean ridge topography, *J. geophys. Res.,* **117**(B4), doi:10.1029/2011JB008765.

Manriquez, P., Contreras-Reyes, E. & Osses, A., 2014. Lithospheric 3-D flexure modelling of the oceanic plate seaward of the trench using variable elastic thickness, *Geophys. J. Int.,* **196**(2), 681–693.

Massell, C.G., 2002. Large-scale structural variation of trench outer slopes and rises, *PhD thesis,* University of California, San Diego.

McNutt, M.K. & Menard, H.W., 1982. Constraints on yield strength in the oceanic lithosphere derived from observations of flexure, *Geophys. J. Int.,* **71**(2), 363–394.

Melosh, H.J., 1978. Dynamic support of the outer rise, *Geophys. Res. Lett.,* **5**(5), 321–324.

Müller, R.D., Sdrolias, M., Gaina, C. & Roest, W.R., 2008. Age, spreading rates, and spreading asymmetry of the world's ocean crust, *Geochem. Geophys. Geosyst.*, **9**(4), doi:10.1029/2007GC001743.

Parsons, B. & Molnar, P., 1976. The origin of outer topographic rises associated with trenches, *Geophys. J. Int.,* **1**(4), 707–712.

Parsons, B. & Sclater, J.G., 1977. An analysis of the variation of ocean floor bathymetry and heat flow with age, *J. geophys. Res.,* **82**(5), 803–827.

Pérez-Gussinyé, M., Swain, C.J., Kirby, J.F. & Lowry, A.R., 2009. Spatial variations of the effective elastic thickness, *Te*, using multitaper spectral estimation and wavelet methods: examples from synthetic data and application to South America, *Geochem. Geophys. Geosyst.*, **10**(4), doi:10.1029/2008GC002229.

Ranero, C.R., Phipps Morgan, J., McIntosh, K. & Reichert, C., 2003. Bending-related faulting and mantle serpentinization at the middle america trench, *Nature,* **425**(6956), 367–373.

Sandwell, D.T., 1984. Thermomechanical evolution of oceanic fracture zones, *J. geophys. Res.,* **89**(B13), 11 401–11 413.

Sandwell, D. & Schubert, G., 1982. Lithospheric flexure at fracture zones, *J. geophys. Res.,* **87**(B6), 4657–4667.

Sandwell, D., Garcia, E., Soofi, K., Wessel, P., Chandler, M. & Smith, W. H.F., 2013. Toward 1-mGal accuracy in global marine gravity from CryoSat-2, Envisat, and Jason-1, *Leading Edge,* **32**(8), 892–899.

Smith, W.H. & Sandwell, D.T., 1997. Global sea floor topography from satellite altimetry and ship depth soundings, *Science,* **277**(5334), 1956–1962.

Tanimoto, T., 1998. State of stress within a bending spherical shell and its implications for subducting lithosphere, *Geophys. J. Int.,* **134**(1), 199–206.

Trefethen, L.N., 2000. *Spectral Methods in MATLAB,* Society for Industrial and Applied Mathematics.

Turcotte, D.L. & Schubert, G., 2002. *Geodynamics,* 2nd edn, Cambridge Univ. Press.

Turcotte, D., McAdoo, D. & Caldwell, J., 1978. An elastic-perfectly plastic analysis of the bending of the lithosphere at a trench, *Tectonophysics,* **47**(3–4), 193–205.

van Wees, J.D. & Cloetingh, S., 1994. A finite-difference technique to incorporate spatial variations in rigidity and planar faults into 3-D models for lithospheric flexure, *Geophys. J. Int.,* **117**(1), 179–195.

Watts, A.B., 2001. *Isostasy and Flexure of the Lithosphere,* Cambridge Univ. Press.

Watts, A.B. & Talwani, M., 1974. Gravity anomalies seaward of deep-sea trenches and their tectonic implications, *Geophys. J. Int.,* **36**(1), 57–90.

Wessel, P., 1996. Analytical solutions for 3-D flexural deformation of semi-infinite elastic plates, *Geophys. J. Int.,* **124**(3), 907–918.

APPENDIX A: EXPRESSING 2-D FLEXURE AS A FREDHOLM INTEGRAL EQUATION OF THE SECOND KIND

Recall that we specified the following decomposition for the plate rigidity $D(x, y)$ in (7) in the main text,

$$D(x, y) = D_0 + D'(x, y). \tag{A1}$$

By its definition as a material parameter, the plate rigidity cannot have a negative value, so a restriction for $D'(x, y)$ is that $D'(x, y) > -D_0$ for all (x, y). If we substitute the above decomposition for D into the governing equation (2),

$$D_0\nabla^2\left(\nabla^2 w\right) + \nabla^2\left[D'\nabla^2 w\right] - (1-\nu)\left[\frac{\partial^2 D'}{\partial x^2}\frac{\partial^2 w}{\partial y^2} - 2\frac{\partial^2 D'}{\partial x\partial y}\frac{\partial^2 w}{\partial x\partial y} + \frac{\partial^2 D'}{\partial y^2}\frac{\partial^2 w}{\partial x^2}\right]$$

$$- N_x\frac{\partial^2 w}{\partial x^2} - 2N_{xy}\frac{\partial^2 w}{\partial x\partial y} - N_y\frac{\partial^2 w}{\partial y^2} + \Delta\rho g w = p. \tag{A2}$$

Eventually, we will express this partial differential equation in the space domain as an integral equation in the wavenumber, or Fourier domain. Formally, the 2-D Fourier transform of a function f is defined as,

$$\mathcal{F}\left[f(\boldsymbol{r})\right] = \hat{f}(\boldsymbol{k}) = \int_X \mathrm{d}S\, f(\boldsymbol{r})\mathrm{e}^{-\mathrm{i}2\pi\boldsymbol{k}\cdot\boldsymbol{r}}. \tag{A3}$$

The surface integral is taken over the entire x–y plane denoted by X. The transformed function $\hat{f}$ is a function of the wave vector $\boldsymbol{k}$, which has components k_x and k_y. In this work, we evaluate (A3) and the corresponding inverse Fourier transform using iterated integrals over x and y, as well as k_x and k_y,

$$\mathcal{F}\left[f(\boldsymbol{r})\right] = \hat{f}(\boldsymbol{k}) = \int_{-\infty}^{+\infty}\int_{-\infty}^{+\infty} \mathrm{d}x\,\mathrm{d}y\, f(x, y)\mathrm{e}^{-\mathrm{i}2\pi(k_x x + k_y y)} \tag{A4}$$

$$\mathcal{F}^{-1}\left[\hat{f}(\boldsymbol{k})\right] = f(\boldsymbol{r}) = \int_{-\infty}^{+\infty}\int_{-\infty}^{+\infty} \mathrm{d}k_x\,\mathrm{d}k_y\, f(k_x, k_y)\mathrm{e}^{\mathrm{i}2\pi(k_x x + k_y y)}. \tag{A5}$$

We assume that D' and w are band-limited functions so that their Fourier transforms exist. These variables can therefore be written using inverse Fourier transforms over the dummy variables (ζ_x, ζ_y) and (s_x, s_y), respectively,

$$D'(x, y) = \int_{-\infty}^{+\infty}\int_{-\infty}^{+\infty} \mathrm{d}\zeta_x\,\mathrm{d}\zeta_y\, \hat{D}'(\zeta_x, \zeta_y)\mathrm{e}^{\mathrm{i}2\pi\left(\zeta_x x + \zeta_y y\right)} \tag{A6}$$

$$w(x, y) = \int_{-\infty}^{+\infty}\int_{-\infty}^{+\infty} \mathrm{d}s_x\,\mathrm{d}s_y\, \hat{w}(s_x, s_y)\mathrm{e}^{\mathrm{i}2\pi\left(s_x x + s_y y\right)}. \tag{A7}$$

The expressions (A6) and (A7) are then substituted in the governing equation (2). After performing this substitution, we interchange the order of integration with respect to ζ_x and s_x and similarly for ζ_y and s_y. This manipulation is valid when the absolute value of the integrands are

finite. Carrying out the successive differentiations over x and y leads to:

$$\int_{-\infty}^{+\infty}\int_{-\infty}^{+\infty} \mathrm{d}s_x\,\mathrm{d}s_y \left\{\left[(2\pi)^4 D_0\left(s_x^2+s_y^2\right)^2+(2\pi)^2\left(N_x s_x^2+2N_{xy}s_x s_y+N_y s_y^2\right)+\Delta\rho g\right]\hat{w}(s_x,s_y)\mathrm{e}^{\mathrm{i}2\pi\left(s_x x+s_y y\right)}\right\}$$

$$+(2\pi)^4\int_{-\infty}^{+\infty}\int_{-\infty}^{+\infty}\int_{-\infty}^{+\infty}\int_{-\infty}^{+\infty}\mathrm{d}s_x\,\mathrm{d}s_y\,\mathrm{d}\zeta_x\,\mathrm{d}\zeta_y\left\{\left[(s_x+\zeta_x)^2+\left(s_y+\zeta_y\right)^2\right]\left(s_x^2+s_y^2\right)\hat{D}'(\zeta_x,\zeta_y)\hat{w}(s_x,s_y)\mathrm{e}^{\mathrm{i}2\pi\left[(s_x+\zeta_x)x+\left(s_y+\zeta_y\right)y\right]}\right\}$$

$$-(2\pi)^4(1-\nu)\int_{-\infty}^{+\infty}\int_{-\infty}^{+\infty}\int_{-\infty}^{+\infty}\int_{-\infty}^{+\infty}\mathrm{d}s_x\,\mathrm{d}s_y\,\mathrm{d}\zeta_x\,\mathrm{d}\zeta_y\left\{\left[s_x^2\zeta_y^2-2s_x\zeta_x s_y\zeta_y+s_y^2\zeta_x^2\right]\hat{D}'(\zeta_x,\zeta_y)\hat{w}(s_x,s_y)\mathrm{e}^{\mathrm{i}2\pi\left[(s_x+\zeta_x)x+\left(s_y+\zeta_y\right)y\right]}\right\}=p(x,y). \tag{A8}$$

All the terms in the above equation are still functions of (x, y) since we are just using integral representations for the terms in the left-hand side (LHS). We can then apply the forward transform (A4) to both sides of the equation and get:

$$\int_{-\infty}^{+\infty}\int_{-\infty}^{+\infty}\mathrm{d}x\,\mathrm{d}y\int_{-\infty}^{+\infty}\int_{-\infty}^{+\infty}\mathrm{d}s_x\,\mathrm{d}s_y\left\{\left\{(2\pi)^4 D_0\left(s_x^2+s_y^2\right)^2+(2\pi)^2\left(N_x s_x^2+2N_{xy}s_x s_y+N_y s_y^2\right)+\Delta\rho g\right\}\hat{w}(s_x,s_y)\mathrm{e}^{\mathrm{i}2\pi\left[(s_x-k_x)x+\left(s_y-k_y\right)y\right]}\right\}$$

$$+(2\pi)^4\int_{-\infty}^{+\infty}\int_{-\infty}^{+\infty}\mathrm{d}x\,\mathrm{d}y\int_{-\infty}^{+\infty}\int_{-\infty}^{+\infty}\int_{-\infty}^{+\infty}\int_{-\infty}^{+\infty}\mathrm{d}s_x\,\mathrm{d}s_y\,\mathrm{d}\zeta_x\,\mathrm{d}\zeta_y\left\{\left[(s_x+\zeta_x)^2+\left(s_y+\zeta_y\right)^2\right]\left(s_x^2+s_y^2\right)\hat{D}'(\zeta_x,\zeta_y)\hat{w}(s_x,s_y)\mathrm{e}^{\mathrm{i}2\pi\left[(s_x+\zeta_x-k_x)x+\left(s_y+\zeta_y-k_y\right)y\right]}\right\}$$

$$-(2\pi)^4(1-\nu)\int_{-\infty}^{+\infty}\int_{-\infty}^{+\infty}\mathrm{d}x\,\mathrm{d}y\int_{-\infty}^{+\infty}\int_{-\infty}^{+\infty}\int_{-\infty}^{+\infty}\int_{-\infty}^{+\infty}\mathrm{d}s_x\,\mathrm{d}s_y\,\mathrm{d}\zeta_x\,\mathrm{d}\zeta_y\left\{\left[s_x^2\zeta_y^2-2s_x\zeta_x s_y\zeta_y+s_y^2\zeta_x^2\right]\right.$$

$$\left.\times\hat{D}'(\zeta_x,\zeta_y)\hat{w}(s_x,s_y)\mathrm{e}^{\mathrm{i}2\pi\left[(s_x+\zeta_x-k_x)x+\left(s_y+\zeta_y-k_y\right)y\right]}\right\}=\hat{p}(k_x,k_y). \tag{A9}$$

From the properties of the Dirac delta distribution, we can write the following relations:

$$\int_{-\infty}^{+\infty}\mathrm{d}x\,\mathrm{e}^{\mathrm{i}2\pi(s_x-k_x)x}=\delta\left(s_x-k_x\right),\qquad\int_{-\infty}^{+\infty}\mathrm{d}x\,\mathrm{e}^{\mathrm{i}2\pi[\zeta_x-(k_x-s_x)]x}=\delta\left[\zeta_x-(k_x-s_x)\right] \tag{A10}$$

$$\int_{-\infty}^{+\infty}\mathrm{d}y\,\mathrm{e}^{\mathrm{i}2\pi\left(s_y-k_y\right)y}=\delta(s_y-k_y),\qquad\int_{-\infty}^{+\infty}\mathrm{d}y\,\mathrm{e}^{\mathrm{i}2\pi\left[\zeta_y-\left(k_y-s_y\right)\right]y}=\delta\left[\zeta_y-\left(k_y-s_y\right)\right]. \tag{A11}$$

We substitute these relations (A10) and (A11) into (A9), and then integrate over s_x and s_y for the first set of integrals, while we integrate over ζ_x, ζ_y for the remaining set of integrals. What remains after invoking the sifting property of the Dirac delta distribution is an equation in the wavenumber domain:

$$\left[(2\pi)^4 D_0\left(k_x^2+k_y^2\right)^2+(2\pi)^2\left(N_x k_x^2+2N_{xy}k_x k_y+N_y k_y^2\right)+\Delta\rho g\right]\hat{w}$$

$$+(2\pi)^4\int_{-\infty}^{+\infty}\int_{-\infty}^{+\infty}\mathrm{d}s_x\,\mathrm{d}s_y\left(k_x^2+k_y^2\right)^2\left(s_x^2+s_y^2\right)^2\hat{D}'(k_x-s_x,k_y-s_y)\hat{w}(s_x,s_y)$$

$$-(2\pi)^4(1-\nu)\int_{-\infty}^{+\infty}\int_{-\infty}^{+\infty}\mathrm{d}s_x\,\mathrm{d}s_y\left\{\left[s_x^2(k_y-s_y)^2-2s_x(k_x-s_x)s_y(k_y-s_y)+s_y^2(k_x-s_x)^2\right]\right.$$

$$\left.\times\hat{D}'(k_x-s_x,k_y-s_y)\hat{w}(s_x,s_y)\right\}=\hat{p}. \tag{A12}$$

Rearranging terms slightly and combining the integrals over s_x and s_y, we see that this can be cast in the form of an integral equation,

$$\left[(2\pi)^4 D_0\left(k_x^2+k_y^2\right)^2+(2\pi)^2\left(N_x k_x^2+2N_{xy}k_x k_y+N_y k_y^2\right)+\Delta\rho g\right]\hat{w}$$

$$=\hat{p}(k_x,k_y)-(2\pi)^4\int_{-\infty}^{+\infty}\int_{-\infty}^{+\infty}\mathrm{d}s_x\,\mathrm{d}s_y\left\{\left(k_x^2+k_y^2\right)^2\left(s_x^2+s_y^2\right)^2-(1-\nu)\left\{s_x^2(k_y-s_y)^2\right.\right.$$

$$\left.\left.-2s_x(k_x-s_x)s_y(k_y-s_y)+s_y^2(k_x-s_x)^2\right\}\hat{D}'(k_x-s_x,k_y-s_y)\hat{w}(s_x,s_y)\right\}. \tag{A13}$$

We can write (A13) compactly by adopting a couple of definitions. First, we recall the form of the response function to uniform rigidity D_0, given in (6). Second, we define the kernel $K(k_x, s_x; k_y, s_y)$ as:

$$K(k_x, s_x; k_y, s_y) = -(2\pi)^4 \hat{\Phi}\Big\{\left(k_x^2 + k_y^2\right)^2 \left(s_x^2 + s_y^2\right)^2 - (1-\nu)s_x^2(k_y - s_y)^2 - 2s_x(k_x - s_x)s_y(k_y - s_y) + s_y^2(k_x - s_x)^2\Big\}$$
$$\times \hat{D}'(k_x - s_x, k_y - s_y). \tag{A14}$$

Using the notations specified by (6) and (A14) enables us to express (A13) in the standard form of a 2-D Fredholm integral equation of the second kind,

$$\hat{w}(k_x, k_y) = \hat{p}(k_x, k_y)\hat{\Phi}(k_x, k_y) + \int_{-\infty}^{+\infty}\int_{-\infty}^{+\infty} \mathrm{d}s_x\, \mathrm{d}s_y\, K(k_x, s_x; k_y, s_y)\hat{w}(s_x, s_y), \tag{A15}$$

where the nonhomogeneous term of the integral equation is $p(k_x, k_y)\hat{\Phi}(k_x, k_y)$, which is identical to the uniform plate solution $\hat{w}_0(k_x, k_y)$ stated in (5). Verifying that (A13) is indeed a Fredholm integral equation of the second kind enables us to refer to the well-developed theory behind these types of equations in establishing the existence and uniqueness of a solution. If a solution $\hat{w}$ can be found in the Fourier domain, then by taking the inverse transform we obtain the desired solution $w(x, y)$ to the governing eq. (2). One method of solving Fredholm integral equations is through successive approximation, and in the following section we describe our implementation of such an iterative algorithm.

APPENDIX B: AN ITERATIVE SCHEME TO SOLVE THE EQUIVALENT INTEGRAL EQUATION

If we consider the Fredholm integral equation of the second kind as expressed in (A15) with kernel (A14), for many forms of D' (and hence $\hat{D}'$), the kernel turns out to be neither symmetric, degenerate, nor separable. This implies that some standard methods of solving integral equations are not feasible for our purposes. Ideally, we want to develop a computational framework for solving thin elastic plate flexure problems involving arbitrary variations in rigidity, valid under some criterion of smoothness. In pursuit of this generality, we resort to an iterative solution method.

A solution to the Fredholm integral equation (A15) can be obtained by starting with a guess for $\hat{w}$, then evaluating the right-hand side (RHS) of the equation. This result is then substituted again into the RHS, giving a new estimate for the solution. The process is repeated until the desired accuracy is reached. We will delve further into the conditions for the convergence of this scheme in the next section. In the meantime, we will be demonstrating the iteration process. Suppose that our guess is $\hat{w} = 0$ for all wavenumbers, and so by substituting this into the RHS of (A15), we get that the first solution is $\hat{w}^{(1)} = \hat{w}_0$. By induction, the nth approximation to the solution of the integral equation is given by

$$\hat{w}^{(n)} = \hat{w}_0 + \int_{-\infty}^{+\infty}\int_{-\infty}^{+\infty} \mathrm{d}s_x\, \mathrm{d}s_y\, K(k_x, s_x; k_y, s_y)\hat{w}^{(n-1)}(s_x, s_y). \tag{B1}$$

At each step of the algorithm, we substitute the kernel as given in (A14), then calculate the integral. This may be done completely in the wavenumber domain. However, as some of the individual terms comprising $K(k_x, s_x; k_y, s_y)$ are in the form of a convolution, they may also be computed as multiplications in the space domain. To see this, we rewrite the integrand by separating it according to the constituent terms of the kernel:

$$\begin{aligned}
&\int_{-\infty}^{+\infty}\int_{-\infty}^{+\infty} \mathrm{d}s_x\, \mathrm{d}s_y\, K(k_x, s_x; k_y, s_y)\hat{w}^{(n-1)}(s_x, s_y) \\
&= -(2\pi)^4 \hat{\Phi}\Bigg\{\left(k_x^2 + k_y^2\right)^2 \int_{-\infty}^{+\infty}\int_{-\infty}^{+\infty} \mathrm{d}s_x\, \mathrm{d}s_y \left[\hat{D}'(k_x - s_x, k_y - s_y)\right]\left[\left(s_x^2 + s_y^2\right)^2 \hat{w}^{(n-1)}(s_x, s_y)\right] \\
&\quad - (1-\nu)\Bigg\{\int_{-\infty}^{+\infty}\int_{-\infty}^{+\infty} \mathrm{d}s_x\, \mathrm{d}s_y \left[(k_y - s_y)^2 \hat{D}'(k_x - s_x, k_y - s_y)\right]\left[s_x^2 \hat{w}^{(n-1)}(s_x, s_y)\right] \\
&\quad - 2\int_{-\infty}^{+\infty}\int_{-\infty}^{+\infty} \mathrm{d}s_x\, \mathrm{d}s_y \left[(k_x - s_x)(k_y - s_y)\hat{D}'(k_x - s_x, k_y - s_y)\right]\left[s_x s_y \hat{w}^{(n-1)}(s_x, s_y)\right] \\
&\quad + \int_{-\infty}^{+\infty}\int_{-\infty}^{+\infty} \mathrm{d}s_x\, \mathrm{d}s_y \left[(k_x - s_x)^2 \hat{D}'(k_x - s_x, k_y - s_y)\right]\left[s_y^2 \hat{w}^{(n-1)}(s_x, s_y)\right]\Bigg\}\Bigg\}.
\end{aligned} \tag{B2}$$

The individual terms on the RHS may be identified as convolutions in the wavenumber domain. By the convolution theorem, these terms have equivalent representations in the space domain. The presence of terms proportional to powers of the wavenumber components suggests that

we are dealing with the derivatives of D' and w. Thus, an alternate way of expressing (B2) is

$$\int_{-\infty}^{+\infty}\int_{-\infty}^{+\infty} \mathrm{d}s_x\,\mathrm{d}s_y\,K(k_x,s_x;k_y,s_y)\hat{w}^{(n-1)}(s_x,s_y)$$
$$= -\hat{\Phi}(k_x,k_y)\mathcal{F}\left\{\nabla^2\left[D'\nabla^2 w^{(n-1)}\right]\right.$$
$$\left.-(1-\nu)\left[\frac{\partial^2 D'}{\partial x^2}\frac{\partial^2 w}{\partial y^2}^{(n-1)} - 2\frac{\partial^2 D'}{\partial x\partial y}\frac{\partial^2 w}{\partial x\partial y}^{(n-1)} + \frac{\partial^2 D'}{\partial y^2}\frac{\partial^2 w}{\partial x^2}^{(n-1)}\right]\right\}. \tag{B3}$$

Substitution of (B3) in (B1) leads to the expression (9) that was presented and discussed in the main body of the paper.

APPENDIX C: CONDITIONS FOR CONVERGENCE OF THE ITERATIVE SOLUTION

The Fredholm theory of integral equations provides a framework for discussing the existence and uniqueness of a solution obtained by an iterative technique. When written in a standard form such as in (A15), the RHS of an integral equation is regarded as an operator $\mathcal{T}$ acting on the unknown function. In our case, the unknown function we are solving for is $\hat{w}$, and the operator $\mathcal{T}[\hat{w}]$ may be defined as,

$$\mathcal{T}[\hat{w}] = \hat{w}_0 + \int_{-\infty}^{+\infty}\int_{-\infty}^{+\infty} \mathrm{d}s_x\,\mathrm{d}s_y\,K(k_x,s_x;k_y,s_y)\hat{w}(s_x,s_y). \tag{C1}$$

In the operator view of integral equations, the Banach fixed point theorem ensures that a unique solution will exist for $\hat{w} = \mathcal{T}[\hat{w}]$ for a contractive mapping $\mathcal{T}$ on a complete metric space (Korevaar 1968; Jerri 1999). Now, the operator $\mathcal{T}$ can be considered to be a contractive mapping on the metric space $\mathcal{M}$ if for each $u_1, u_2 \in \mathcal{M}$ the following relation holds,

$$\mathrm{d}[\mathcal{T}(u_1),\mathcal{T}(u_2)] \le \Upsilon d(u_1,u_2). \tag{C2}$$

In the above condition, $0 < \Upsilon < 1$, and the metric d between two continuous functions $u_1(\boldsymbol{k})$ and $u_2(\boldsymbol{k})$ in the set $\mathcal{C}[(\xi_a,\xi_b);(\eta_a,\eta_b)]$ is defined as

$$\mathrm{d}[u_1(k_x,k_y),u_2(k_x,k_y)] = \max_{(k_x,k_y)\in[(\xi_a,\xi_b);(\eta_a,\eta_b)]}\left|u_1[(k_x,k_y),u_2(k_x,k_y)] - u_2[(k_x,k_y),u_2(k_x,k_y)]\right|. \tag{C3}$$

Before we evaluate the criterion (C2) as it applies to consecutive estimates of $\hat{w}$ resulting from the iterations, we make a few more assumptions. First, $\hat{w}_0$ must be continuous over the region described by $(k_x,k_y)\in[(\xi_a,\xi_b);(\eta_a,\eta_b)]$. The kernel $K(k_x,s_x;k_y,s_y)$ must also be continuous in $\{(k_x,s_x;k_y,s_y) : (k_x,k_y)\in[(\xi_a,\xi_b);(\eta_a,\eta_b)], (s_x,s_y)\in[(\xi_a,\xi_b);(\eta_a,\eta_b)]\}$. Furthermore, the kernel must be bounded such that $|K(k_x,s_x;k_y,s_y)| < \vartheta$ where ϑ is some finite constant. Note that these assumptions are consistent with our previously set requirements that the Fourier transforms of the load distribution p and rigidity D must exist, and furthermore band-limited.

Considering the LHS of (C2) as it applies to successive estimates for $\hat{w}$, we get

$$\mathrm{d}[\mathcal{T}(\hat{w}_{n+1}),\mathcal{T}(\hat{w}_n)] = \max_{(k_x,k_y)\in[(\xi_a,\xi_b);(\eta_a,\eta_b)]}\left|\hat{w}_0 + \int_{\xi_a}^{\xi_b}\int_{\eta_a}^{\eta_b}\mathrm{d}s_x\,\mathrm{d}s_y\,K(k_x,s_x;k_y,s_y)\hat{w}^{(n+1)}(s_x,s_y)\right.$$
$$\left.-\hat{w}_0 - \int_{\xi_a}^{\xi_b}\int_{\eta_a}^{\eta_b}\mathrm{d}s_x\,\mathrm{d}s_y\,K(k_x,s_x;k_y,s_y)\hat{w}^{(n)}(s_x,s_y)\right|$$
$$\mathrm{d}[\mathcal{T}(\hat{w}_{n+1}),\mathcal{T}(\hat{w}_n)] = \max_{(k_x,k_y)\in[(\xi_a,\xi_b);(\eta_a,\eta_b)]}\left|\int_{\xi_a}^{\xi_b}\int_{\eta_a}^{\eta_b}\mathrm{d}s_x\,\mathrm{d}s_y\,K(k_x,s_x;k_y,s_y)\left[\hat{w}^{(n)}(s_x,s_y) - \hat{w}^{(n+1)}(s_x,s_y)\right)\right]\right|. \tag{C4}$$

Meanwhile, it may be shown that the RHS fulfills the inequality

$$\max_{(k_x,k_y)\in[(\xi_a,\xi_b);(\eta_a,\eta_b)]}\left|\int_{\xi_a}^{\xi_b}\int_{\eta_a}^{\eta_b}\mathrm{d}s_x\,\mathrm{d}s_y\,K(k_x,s_x;k_y,s_y)\left[\hat{w}^{(n)}(s_x,s_y) - \hat{w}^{(n+1)}(s_x,s_y)\right)\right]\right|$$
$$\le \max_{(k_x,k_y)\in[(\xi_a,\xi_b);(\eta_a,\eta_b)]}\left|\hat{w}^{(n)}(s_x,s_y) - \hat{w}^{(n+1)}(s_x,s_y)\right)\right| \max_{(k_x,k_y)\in[(\xi_a,\xi_b);(\eta_a,\eta_b)]}\int_{\xi_a}^{\xi_b}\int_{\eta_a}^{\eta_b}\mathrm{d}s_x\,\mathrm{d}s_y\left|K(k_x,s_x;k_y,s_y)\right|$$
$$\max_{(k_x,k_y)\in[(\xi_a,\xi_b);(\eta_a,\eta_b)]}\left|\int_{\xi_a}^{\xi_b}\int_{\eta_a}^{\eta_b}\mathrm{d}s_x\,\mathrm{d}s_y\,K(k_x,s_x;k_y,s_y)\left[\hat{w}^{(n)}(s_x,s_y) - \hat{w}^{(n+1)}(s_x,s_y)\right)\right]\right|$$
$$\le d\left(\hat{w}^{(n+1)},\hat{w}^{(n)}\right)\max_{(k_x,k_y)\in[(\xi_a,\xi_b);(\eta_a,\eta_b)]}\int_{\xi_a}^{\xi_b}\int_{\eta_a}^{\eta_b}\mathrm{d}s_x\,\mathrm{d}s_y\,|K(k_x,s_x;k_y,s_y)| \tag{C5}$$

as in (Korevaar 1968) and following the definition of the metric (C3). If we compare the RHS of (C2) with the required convergence criteria for this case, which is

$$d\left(\mathcal{T}(\hat{w}^{(n+1)}), \mathcal{T}(\hat{w}^{(n)})\right) \leq \Upsilon d\left(\hat{w}^{(n+1)}, \hat{w}^{(n)}\right) \tag{C6}$$

then $\Upsilon = \max_{(k_x,k_y)\in[(\xi_a,\xi_b);(\eta_a,\eta_b)]} \int_{\xi_a}^{\xi_b} \int_{\eta_a}^{\eta_b} \mathrm{d}s_x \, \mathrm{d}s_y \, |K(k_x, s_x; k_y, s_y)|$ and so the condition for convergence is just

$$\max_{(k_x,k_y)\in[(\xi_a,\xi_b);(\eta_a,\eta_b)]} \int_{\xi_a}^{\xi_b} \int_{\eta_a}^{\eta_b} \mathrm{d}s_x \, \mathrm{d}s_y \, |K(k_x, s_x; k_y, s_y)| < 1. \tag{C7}$$

Thus, for a fixed point to exist and for the iterative scheme to converge, the maximum of the integral of the absolute value of the kernel over the wavenumber bands of interest must be a sufficiently small value. The implication for the form of D and q in the space domain is that they must be smoothly varying functions over a narrow range of spatial scales.

APPENDIX D: APPROXIMATING APPLIED MOMENTS WITH VERTICAL LOAD COUPLES

Following an approximation that may be taken for infinite 1-D beams (Hetenyi 1946; Watts 2001), we also tested how well a moment along the x-direction M_0 applied to an interior point of the plate can be represented as a pair of opposing vertical loads V_0 separated by an infinitesimal distance Δx (Fig. D1). This may be expressed formally as,

$$M_0 \approx \lim_{\Delta x \to 0} V_0 \Delta x. \tag{D1}$$

Since the system (2) is linear, the solution for the deflection w due to two opposing loads is simply the superposition of the individual solutions for each of the loads. Thus, in 1-D, if $+V$ is applied at $x = 0$ and $-V$ at $x = \Delta x$, and if we refer to the solution in the line load case (10) as w_V, then solution for this load couple w_c is given by the sum

$$w_M = w_V(x + \Delta x) - w_V(x). \tag{D2}$$

Rewriting this expression slightly,

$$w_M = \Delta x \frac{w_V(x + \Delta x) - w_V(x)}{\Delta x}. \tag{D3}$$

Thus, as Δx becomes small,

$$w_M = \Delta x \lim_{\Delta x \to 0} \frac{w_V(x + \Delta x) - w_V(x)}{\Delta x} \approx \Delta x \frac{\partial w_V}{\partial x}. \tag{D4}$$

Recalling (10) and taking its derivative along x, we get

$$w_M(x) = -\frac{V \Delta x \alpha^2}{4D_0} \exp\left(-\frac{|x|}{\alpha}\right) \sin\left(\frac{x}{\alpha}\right) \approx -\frac{M_0 \alpha^2}{4D_0} \exp\left(-\frac{|x|}{\alpha}\right) \sin\left(\frac{x}{\alpha}\right) \tag{D5}$$

following our assumption that $V\Delta x$ approaches M_0. Thus, the approximate solution for an applied moment M_0 is (Hetenyi 1946)

$$w = -w_m \exp\left(-\frac{|x|}{\alpha}\right) \sin\left(\frac{x}{\alpha}\right), \tag{D6}$$

where $w_m = M_0\alpha^2/4D_0$, which is included in the main text as eq. (17).

We may apply the same set of assumptions to obtain an expression for the deflection due to a concentrated moment on a 2-D infinite plate. First, recall that the solution w for a point load with amplitude V_0 can be written in terms of the Kelvin–Bessel function Kei of order zero as (Brotchie 1971; Lambeck & Nakiboglu 1980)

$$w = w_p \mathrm{Kei}_0\left[\frac{\left(x^2 + y^2\right)^{1/2}}{l}\right], \tag{D7}$$

where $w_p = V_0 l^2/2\pi D_0$ and the flexural parameter l is

$$l = \left[\frac{D_0}{\Delta\rho g}\right]^{1/4}. \tag{D8}$$

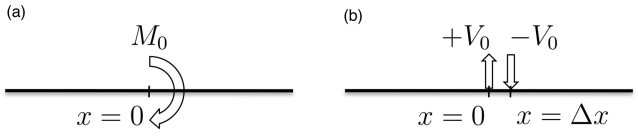

Figure D1. (a) A clockwise moment M_0 is applied at the origin. (b) The flexural deflection due to M_0 may be approximated as being due to the superposition of two opposing loads of equal magnitude V_0 placed a small distance Δx apart.

By taking the partial derivative with respect to x of (D7), the solution for a concentrated moment aligned with the x-axis is

$$w = w_r \left\{ \mathrm{Kei}_1 \left[\frac{\left(x^2 + y^2\right)^{1/2}}{l} \right] - \mathrm{Ker}_1 \left[\frac{\left(x^2 + y^2\right)^{1/2}}{l} \right] \right\}, \tag{D9}$$

where we are using Kelvin–Bessel functions Ker and Kei of order 1, and $w_r = w_p[x/2^{1/2}l(x^2 + y^2)^{1/2}]$. This is also included in the main text as eq. (19).

APPENDIX E: EXPRESSIONS FOR THE SOLUTION OF A LINE MOMENT APPLIED TO A PLATE WITH PIECEWISE RIGIDITY

We derive the analytic solution for deflection produced by a line moment applied to a plate with a sharp step in flexural rigidity such that

$$D(x) = \begin{cases} D_1 : & x < 0 \\ D_2 : & x > 0 \end{cases} \tag{E1}$$

following the approach of (Sandwell & Schubert 1982). In the absence of in-plane forces, the governing equations may be written as a coupled system:

$$D_1 \frac{d^4 w_1}{\mathrm{d}x^4} + \Delta\rho g w_1 = 0 : \quad x > 0 \tag{E2}$$

$$D_2 \frac{d^4 w_2}{\mathrm{d}x^4} + \Delta\rho g w_2 = 0 : \quad x < 0. \tag{E3}$$

The boundary conditions are that the deflections w_1, w_2 and their slopes vanish as $|x| \to \infty$. The general solutions in each region of the plate have the form

$$w_1 = \exp\left(\frac{x}{\alpha_1}\right)\left[A_1 \cos\left(\frac{x}{\alpha_1}\right) + B_1 \sin\left(\frac{x}{\alpha_1}\right)\right] : \quad x < 0 \tag{E4}$$

$$w_2 = \exp\left(-\frac{x}{\alpha_2}\right)\left[A_2 \cos\left(\frac{x}{\alpha_2}\right) + B_2 \sin\left(\frac{x}{\alpha_2}\right)\right] : \quad x > 0. \tag{E5}$$

Note that the flexural parameters α_1 and α_2 are different for each region,

$$\alpha_{1,2} = \left[\frac{4D_{1,2}}{\Delta\rho g}\right]^{1/4}. \tag{E6}$$

The plate is subject to a line moment applied at $x = 0$. Apart from the boundary conditions at the edges of the model, the following matching conditions must also be fulfilled at the discontinuity in rigidity (also at $x = 0$):

$$w_1 - w_2 = 0 \tag{E7}$$

$$\frac{\mathrm{d}w_1}{\mathrm{d}x} - \frac{\mathrm{d}w_2}{\mathrm{d}x} = 0 \tag{E8}$$

$$-D_1 \frac{d^2 w_1}{\mathrm{d}x^2} - D_2 \frac{d^2 w_2}{\mathrm{d}x^2} = M_0 \tag{E9}$$

$$-D_1 \frac{d^3 w_1}{\mathrm{d}x^3} - D_2 \frac{d^3 w_2}{\mathrm{d}x^3} = 0. \tag{E10}$$

These matching conditions ensure the continuity of the deflections, slopes, and shear forces. The third condition accounts for the applied moment at the origin. Solving the linear system resulting from these matching conditions leads to explicit expressions for the unknown coefficients A_1, B_1, A_2 and B_2 in (E4)–(E5).

In our solution, we found that $A_1 = A_2 = A$, which may be expressed in terms of the flexural parameters $\alpha_{1,2}$ and the moment M_0 as

$$A = -\frac{\frac{1}{\alpha_1}\left(1 + \frac{\alpha_1}{D_1}\frac{D_2}{\alpha_2}\right) - \frac{\alpha_1}{D_1}\frac{D_2}{\alpha_2}\left(\frac{1}{\alpha_1} + \frac{1}{\alpha_2}\right)}{\left(\frac{D_1}{\alpha_1^3} + \frac{D_1}{\alpha_2^3}\right)\left(1 + \frac{\alpha_1}{D_1}\frac{D_2}{\alpha_2}\right) + \frac{D_2}{\alpha_2}\left(\frac{1}{\alpha_1} + \frac{1}{\alpha_2}\right)^2}\left(\frac{M_0}{2}\right). \tag{E11}$$

The respective expressions for B_1 and B_2 are

$$B_1 = \frac{\alpha_1^2}{D_1}\left(\frac{M_0}{2} + \frac{D_2}{\alpha_2^2}B_2\right) \tag{E12}$$

$$B_2 = \frac{\alpha_2\left[\frac{\alpha_1}{D_1}\frac{M_0}{2} + \left(\frac{1}{\alpha_1} + \frac{1}{\alpha_2}\right)A\right]}{\left(1 + \frac{\alpha_1}{D_1}\frac{D_2}{\alpha_2}\right)}. \tag{E13}$$